



Fluorine-doped Bi_2O_3 derived from metal-organic framework for electrocatalytic CO_2 reduction to formate at industrial current densities

Yue Qiao, Yue Xu, Junquan Yang, Junfang Ding*, Xiaojun Gu*

Keywords:

CO_2 electroreduction, Bi_2O_3 , doping, formate, oxygen vacancy

Citation:

Qiao, Y.; Xu, Y.; Yang, J.; Ding, J.; Gu, X. Fluorine-doped Bi_2O_3 derived from metal-organic framework for electrocatalytic CO_2 reduction to formate at industrial current densities. *Energy Mater.* 2026, 6, 600047. <https://dx.doi.org/10.20517/energymater.2026.07>

Received: 17 Jan 2026

First Decision: 2 Mar 2026

Revised: 20 Mar 2026

Accepted: 16 Apr 2026

Published: 7 May 2026

Academic Editor:

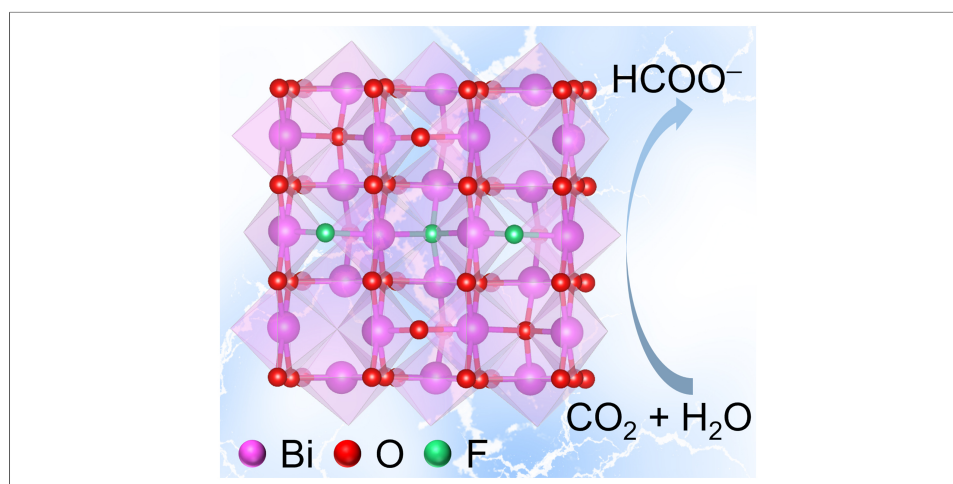
Hao Liu

Copy Editor:

Fangling Lan

Production Editor:

Fangling Lan



Abstract

Achieving high activity and stability at high current densities is critical in the practical application of electrocatalytic CO_2 reduction (ECO_2R). In this study, a fluorine-doped Bi_2O_3 electrocatalyst with oxygen vacancies (denoted as $\text{F-Bi}_2\text{O}_3\text{-O}_v$) has been synthesized using a Bi-based metal-organic framework as the sacrificial template. Catalyst characterizations reveal that the fluorine doping induces results in lattice expansion and generates abundant oxygen vacancies. The $\text{F-Bi}_2\text{O}_3\text{-O}_v$ catalyst delivers a formate Faradaic efficiency of 94% at a current density of 300 mA cm^{-2} and with stable performance for over 25 h in a flow cell. Electrochemical kinetics analysis and *in situ* attenuated total reflectance Fourier transform infrared spectroscopy establish a fluorine doping and oxygen vacancies synergy that facilitates interfacial charge transfer, lowering the energy barrier for the formation of the key $^*\text{OCHO}$ intermediate. The findings of this study offer an effective strategy for modulating the electronic and geometric characteristics of metal oxide catalysts for high-performance ECO_2R .



School of Chemistry and Chemical Engineering, Inner Mongolia Key Laboratory of Low Carbon Catalysis, Inner Mongolia University, Hohhot 010021, Inner Mongolia, China.

*Correspondence to: Dr. Junfang Ding, Dr. Xiaojun Gu, School of Chemistry and Chemical Engineering, Inner Mongolia Key Laboratory of Low Carbon Catalysis, Inner Mongolia University, Hohhot 010021, Inner Mongolia, China. E-mail: dingjf@imu.edu.cn; xiaojun.gu@imu.edu.cn

INTRODUCTION

Electrocatalytic CO₂ reduction (ECO₂R) powered by renewable electricity represents a sustainable process that mitigates greenhouse gas emissions in the production of value-added chemicals^[1–4]. Formate, as a target reduction product, is recognized as a highly promising liquid hydrogen carrier and feedstock for direct formic acid fuel cells, offering high volumetric capacity and economic viability^[5–7]. Consequently, the development of efficient electrocatalysts for the selective conversion of CO₂ to formate at industrially relevant current densities is a critical research goal. Bismuth-based materials have emerged as promising candidates for formate production due to their non-toxicity, low cost and unique electronic structure that stabilizes the key intermediate (*OCHO)^[8–10]. In particular, bismuth(III) oxide (Bi₂O₃) has demonstrated high intrinsic activity for formate generation^[11,12]. However, bulk Bi₂O₃ catalysts are known to have a low electrical conductivity, limited active site exposure and poor structural stability under reductive potentials. These limitations result in low current densities and rapid decay in Faradaic efficiency (FE) during long-term operation, particularly at high reaction rates and severe competition from the hydrogen evolution reaction (HER)^[13,14]. In order to overcome these obstacles, a simultaneous modulation of the electronic structure and morphological engineering is required to enhance both catalyst activity and durability^[15,16].

Defect engineering and heteroatom doping are effective strategies to optimize the intrinsic catalytic properties of metal oxides^[17–21]. Introducing oxygen vacancies (O_v) can generate unsaturated coordination sites that facilitate CO₂ adsorption and charge transfer^[22,23]. Furthermore, doping with high-electronegativity anions, such as fluorine, can induce strong charge polarization and lattice distortion^[24]. In theory, the incorporation of fluorine modulates the p-orbital electron density of Bi centers and optimizes the intermediate binding energy while also promoting the formation of oxygen vacancies, creating a synergistic environment for CO₂ activation^[25,26]. Moreover, the fabrication of catalysts from metal-organic frameworks (MOFs) offers distinct structural advantages^[27–29]. The inherent porosity and periodic metal centers that characterize MOFs enable the synthesis of derivative oxides, which maximize the exposure of active sites and facilitate mass transport at high current densities^[30–32].

In this study, we report the synthesis of fluorine-doped Bi₂O₃ catalysts with abundant oxygen vacancies (denoted as F-Bi₂O₃-O_v) via the fluoride-assisted pyrolysis of a Bi-based MOF (denoted as Bi-MOF). The optimized fluorine-doped Bi₂O₃ catalyst for electrocatalytic CO₂ reduction provides a remarkable formate FE of 94% at a current density of 300 mA cm⁻² in a flow cell operation. Fluorine doping causes Bi₂O₃ lattice expansion, generating more oxygen vacancies and enhancing the stability of the Bi³⁺ active sites. A combined theoretical simulation and experimental testing has demonstrated a synergism associated with oxygen vacancies and fluorine doping that promotes the hydrogenation of the *OCHO intermediate with a consequent efficient conversion of CO₂ to formate at industrial-grade current densities.

EXPERIMENTAL

Materials

Bismuth nitrate pentahydrate (Bi(NO₃)₃·5H₂O, 99.0%) was purchased from Tianjin Fengchuan Chemical Reagent Technology Co., Ltd. 1,3,5-benzenetricarboxylic acid (H₃BTC, 98%) was purchased from Shandong Kexuan Biochemical Co., Ltd. Methanol (CH₃OH, 99.5%) was purchased from Tianjin Xintebote Chemical Co., Ltd. Sodium fluoride (NaF, 99.99%) was purchased from Shanghai McLyn Biochemical Technology Co., Ltd. Deuterium oxide (D₂O, 99.9%) and dimethyl sulfoxide (DMSO, 99.9%) were purchased from Beijing Innochem Science & Technology Co., Ltd. Sodium fluoride (NaF, 99.99%) was purchased from Shanghai McLyn Biochemical Technology Co., Ltd. Ultrapure water was used in all the experiments with a resistivity of 18.2 MΩ·cm⁻¹. The gas diffusion layer (GDL, Sigracet 38 BC) was purchased from Wuhan Gaoshi Ruilian Technology Co., Ltd. The anion exchange membrane (FAB-PK-130) was purchased from FuMA Technology

Co., Ltd. A Nafion solution (5 wt%) was purchased from Suzhou Shengernuo Technology Co., Ltd. High-purity argon (Ar, 99.99%), high-purity nitrogen (N_2 , 99.999%) and high-purity carbon dioxide (CO_2 , 99.999%) were used in all experiments. All the chemicals were used as supplied without further purification.

Catalyst preparation

Synthesis of Bi-MOF

$Bi(NO_3)_3 \cdot 5H_2O$ (150 mg) and H_3BTC (750 mg) were dissolved in methanol (60 mL) and stirred for 30 min. The resulting solution was transferred into a 100 mL Teflon-lined autoclave and heated at 120 °C for 24 h. After the reaction, the product was collected by centrifugation and washed with methanol.

Synthesis of $F-Bi_2O_3-O_v$

A mixture of Bi-MOF (20 mg) and NaF (2 mg) was placed in a tube furnace, and heated to 450 °C for 6 h at 5 °C·min⁻¹ in air, and then cooled to room temperature to obtain $F-Bi_2O_3-O_v$.

Synthesis of $0.5F-Bi_2O_3-O_v$

The sample was synthesized using a similar procedure to that employed for $F-Bi_2O_3-O_v$, but utilizing 1 mg NaF.

Synthesis of $2F-Bi_2O_3-O_v$

The sample was synthesized using a similar procedure to that employed for $F-Bi_2O_3-O_v$, but utilizing 4 mg NaF.

Synthesis of $Bi_2O_3-O_v$

The sample was synthesized using a similar procedure to that employed for $F-Bi_2O_3-O_v$, without the inclusion of NaF.

Synthesis of Bi_2O_3

$Bi(NO_3)_3 \cdot 5H_2O$ (200 mg) was placed in a muffle furnace, and heated to 450 °C for 6 h at 5 °C·min⁻¹ in air. The resulting product was cooled to room temperature to obtain Bi_2O_3 .

Synthesis of $F-Bi_2O_3$

The sample was synthesized using a similar procedure to that employed for $F-Bi_2O_3-O_v$, substituting Bi-MOF with Bi_2O_3 .

Characterization

X-ray diffraction (XRD) analyses were performed on a Bruker D8 ADVANCE X-ray diffractometer with Cu $K\alpha$ radiation at 40 kV and 40 mA. Scanning electron microscopy (SEM) analyses were conducted using a Hitachi S4800 microscope. Transmission electron microscope (TEM), high-resolution TEM (HRTEM) and energy-dispersive spectroscopy were performed on a FEI TECNAI G2 F20 microscope. X-ray photoelectron spectroscopy (XPS) analyses were carried out on a Thermo Scientific ESCALAB 250Xi unit equipped with an Al- $K\alpha$ X-ray excitation source. Nitrogen adsorption-desorption isotherm measurements were carried out on a Micromeritics ASAP 2460 unit. Thermogravimetric analysis (TGA) was performed on a TA Q5000IR TGA thermal analyzer. The chemical composition was determined by inductively coupled plasma optical emission spectrometry (ICP-OES), using an Agilent 5110 unit. Electron paramagnetic resonance (EPR) spectra were performed on a Bruker EMXplus 10/12 unit equipped with an Oxford ESR910 Liquid Helium cryostat. Raman spectra were recorded on a Horiba LabRAM HR Evolution Raman microscope with a laser excitation

source of 532 nm. *In situ* attenuated total reflectance Fourier transform infrared spectroscopy (ATR-FTIR) analyses were performed on a Nicolet iS 50 spectrometer (Thermo Fisher) equipped with a liquid nitrogen-cooled MCT detector. The liquid products were analyzed using a Bruker AVANCE NEO 600 MHz ^1H NMR spectrometer. The gaseous products were analyzed by gas chromatography (GC) using a GC-2014 chromatograph (Shimadzu Corporation, Japan). Electrochemical measurements were conducted using an electrochemical workstation (CHI 1140D, Shanghai Chenhua Instrument Co., Ltd., Shanghai, China).

RESULTS AND DISCUSSION

The preparation of the $\text{F-Bi}_2\text{O}_3\text{-O}_\text{v}$ catalyst is illustrated in Figure 1A. The Bi-MOF precursor was synthesized under solvothermal conditions, as confirmed by the XRD, SEM and TEM analyses [Supplementary Figures 1-3]. The N_2 adsorption isotherm analysis establishes that the Bi-MOF has a porous structure [Supplementary Figure 4]. The optimal pyrolysis temperature was determined by TGA conducted in air [Supplementary Figure 5]. The TGA curve confirms that the organic ligands are completely decomposed at 380 °C. Consequently, 450 °C was selected as the pyrolysis temperature to ensure a complete removal of the organic components. The Bi-MOF was pyrolyzed with NaF at 450 °C to produce $\text{F-Bi}_2\text{O}_3\text{-O}_\text{v}$. For comparison, three reference samples were considered, including the Bi-MOF-derived catalyst without fluorine (denoted as $\text{Bi}_2\text{O}_3\text{-O}_\text{v}$), bulk Bi_2O_3 obtained via direct calcination of $\text{Bi}(\text{NO}_3)_3 \cdot 5\text{H}_2\text{O}$ and $\text{F-Bi}_2\text{O}_3$ prepared by direct fluorination of Bi_2O_3 . The XRD analysis reveals that $\text{F-Bi}_2\text{O}_3\text{-O}_\text{v}$ and $\text{Bi}_2\text{O}_3\text{-O}_\text{v}$ exhibit analogous structure features [Figure 1B]. Following fluorine doping, the (221) diffraction peak for $\text{F-Bi}_2\text{O}_3\text{-O}_\text{v}$ is shifted slightly to a lower angle when compared with $\text{Bi}_2\text{O}_3\text{-O}_\text{v}$, suggesting a lattice expansion due to the incorporation of fluorine [Figure 1C]. This response may be attributed to the formation of oxygen vacancies facilitated by fluorine doping, which results in a local lattice distortion^[33]. The SEM images demonstrate that the $\text{Bi}_2\text{O}_3\text{-O}_\text{v}$ and $\text{F-Bi}_2\text{O}_3\text{-O}_\text{v}$ catalysts exhibit flake-like or granular morphologies with an intrinsic porosity, whereas Bi_2O_3 obtained from direct calcination forms larger (1-2 μm) aggregates [Supplementary Figures 6-8]. The MOF-mediated synthesis generates higher surface areas for $\text{F-Bi}_2\text{O}_3\text{-O}_\text{v}$ and $\text{Bi}_2\text{O}_3\text{-O}_\text{v}$ relative to pure Bi_2O_3 [Supplementary Figure 9]. Selected-area electron diffraction (SAED) patterns for $\text{Bi}_2\text{O}_3\text{-O}_\text{v}$ and $\text{F-Bi}_2\text{O}_3\text{-O}_\text{v}$ [Supplementary Figures 10 and 11] reveal that the (221) crystal plane is the predominantly exposed facet of the Bi_2O_3 phase. High-resolution TEM (HRTEM) images [Figure 1D and E] show that the lattice spacing of the (221) planes increases from 0.32 nm in $\text{Bi}_2\text{O}_3\text{-O}_\text{v}$ to 0.34 nm in $\text{F-Bi}_2\text{O}_3\text{-O}_\text{v}$, consistent with the lattice expansion observed in the XRD analysis. Moreover, the bulk Bi_2O_3 exhibits lattice fringes of 0.24, 0.34 and 0.27 nm, corresponding to the (330), (310) and (330) planes, respectively [Supplementary Figure 12]. The elemental maps [Figure 1F] show a homogeneous distribution of Bi, O and F elements in $\text{F-Bi}_2\text{O}_3\text{-O}_\text{v}$. The content (6.66 wt%) of fluorine by the ion-selective electrode measurement establishes a structural modulation due to fluorination. In addition, the elemental maps of $\text{Bi}_2\text{O}_3\text{-O}_\text{v}$ and Bi_2O_3 demonstrate a uniform distribution of Bi and O elements [Supplementary Figures 13 and 14].

The XPS measurements were conducted to determine the elemental chemical states of elements in the as-synthesized catalysts. In the high-resolution Bi 4f spectra [Figure 2A and Supplementary Figure 15], the two peaks at 158.6 and 163.8 eV are assigned to $\text{Bi } 4\text{f}_{7/2}$ and $\text{Bi } 4\text{f}_{5/2}$ spin-orbit, respectively^[34]. Following fluorine doping, the Bi peak is shifted by 0.1 eV to a lower binding energy, primarily due to the introduction of more oxygen vacancies by fluorine doping. This facilitates an efficient electron transfer to the metal cations. The F 1s spectra exhibit a dominant peak at 685.7 eV, attributed to the Bi-F bond. The peak at 680.4 eV is assigned to the Bi 4p orbital of Bi^{3+} [Supplementary Figure 16]^[24]. The O 1s spectra can be deconvoluted into three peaks at 529.2, 530.8 and 532.3 eV, that correspond to the lattice oxygen (Bi-O), oxygen vacancies and adsorbed oxygen species, respectively [Figure 2B and Supplementary Figure 17]^[35]. The quantitative analysis reveals that the concentration of oxygen vacancies increases from Bi_2O_3 to $\text{Bi}_2\text{O}_3\text{-O}_\text{v}$,

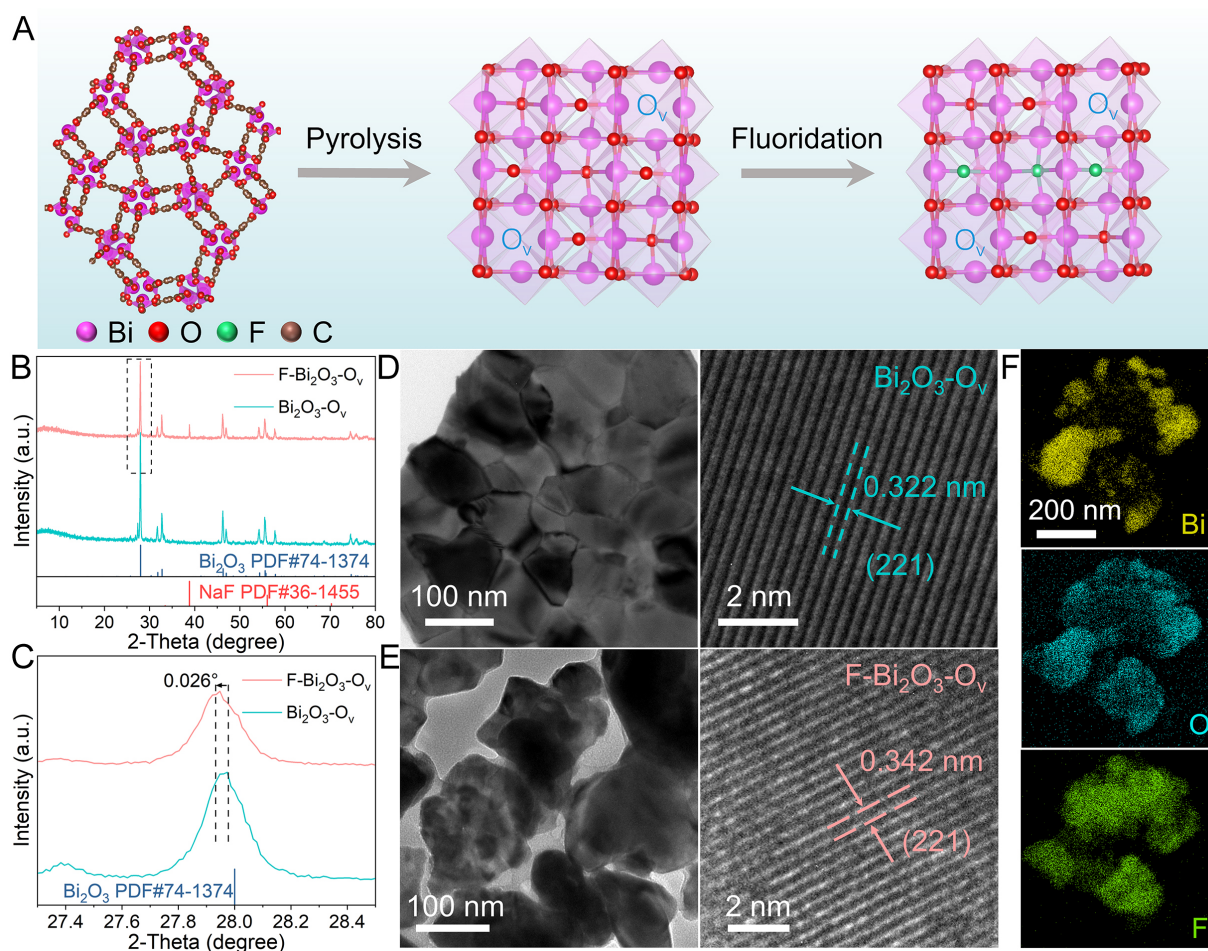


Figure 1. (A) Schematic diagram of the catalyst synthesis. (B) XRD patterns of Bi₂O₃-O_v and F-Bi₂O₃-O_v and (C) the enlarged patterns. TEM and HRTEM images of (D) Bi₂O₃-O_v and (E) F-Bi₂O₃-O_v. (F) Elemental maps for F-Bi₂O₃-O_v.

reaching the highest level in F-Bi₂O₃-O_v [Supplementary Figure 18]. The introduction of oxygen vacancies serves to modify the local Bi electronic environment, promoting CO₂ adsorption and activation. These findings are confirmed by the EPR analysis where the signal at $g = 2.003$ [Figure 2C] is associated with the presence of oxygen vacancies which are generated by fluorination^[36,37]. In addition, the Raman spectra [Figure 2D] show that the peaks located at 95, 127 and 461 cm⁻¹ are assigned to the vibration of Bi-O bonds for Bi₂O₃^[38]. Collectively, these results confirm that fluorine doping results in lattice expansion while also promoting the formation of oxygen vacancies, which establishes a defective and electronically modulated structure that impacts the associated electrochemical properties.

The ECO₂R performance of the Bi₂O₃, Bi₂O₃-O_v and F-Bi₂O₃-O_v catalysts was evaluated in a flow cell. Linear sweep voltammetry (LSV) results reveal that all the catalysts have significantly higher current densities in a CO₂-saturated electrolyte than observed in an Ar-saturated electrolyte at identical potentials [Supplementary Figure 19]. It should be noted that F-Bi₂O₃-O_v exhibits the most pronounced response [Figure 3A], suggesting a superior intrinsic ECO₂R activity. Product analysis identifies formate as the principal liquid product [Supplementary Figures 20–22]. While the three catalysts demonstrate high formate selectivity at current densities below 200 mA cm⁻², the superior performance of F-Bi₂O₃-O_v is evident under high-current conditions. The FE associated with formate on F-Bi₂O₃-O_v reaches 94% at a current density of 300 mA cm⁻², surpassing Bi₂O₃-O_v (85%) and Bi₂O₃ (45%) [Figure 3B]. Moreover, the F-Bi₂O₃-O_v catalyst maintains a superior formate partial current density across the entire potential range. The incorporation of

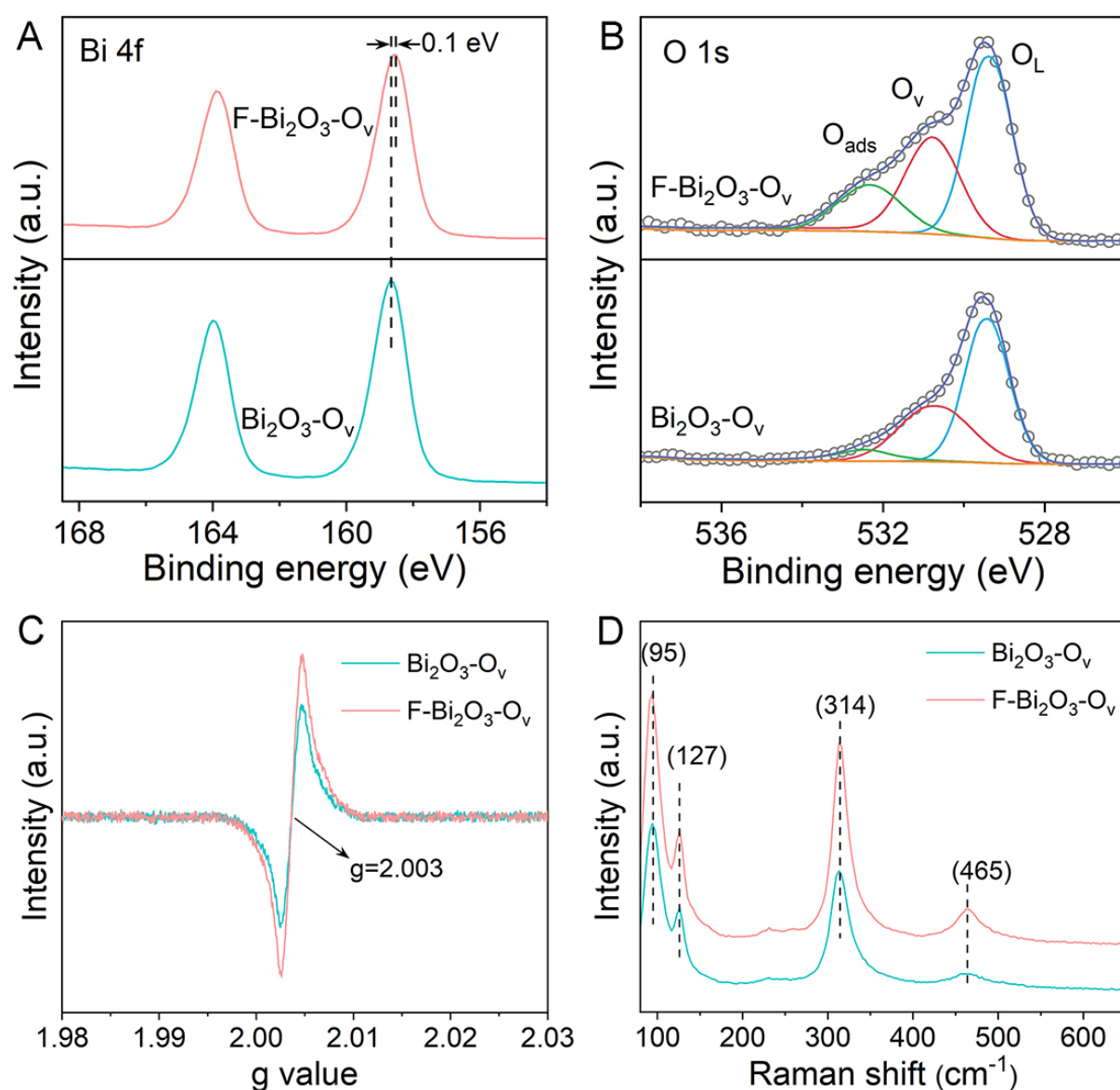


Figure 2. XPS spectra of (A) Bi 4f and (B) O 1s for $\text{Bi}_2\text{O}_3\text{-O}_v$ and $\text{F-Bi}_2\text{O}_3\text{-O}_v$. (C) EPR and (D) Raman spectra for $\text{Bi}_2\text{O}_3\text{-O}_v$ and $\text{F-Bi}_2\text{O}_3\text{-O}_v$.

highly electronegative fluorine in $\text{F-Bi}_2\text{O}_3\text{-O}_v$ facilitates the stabilization of Bi^{3+} as the active site, preventing the recombination of lattice oxygen vacancies under reducing potentials. Consequently, the HER is suppressed. At a total current density of 500 mA cm^{-2} , the formate partial current density for $\text{F-Bi}_2\text{O}_3\text{-O}_v$ reaches 443 mA cm^{-2} , approximately three times higher than that of Bi_2O_3 (147 mA cm^{-2}) [Figure 3C]. In evaluating the direct pyrolysis route using Bi_2O_3 and NaF [Supplementary Figure 23], the results confirm that the enhanced catalytic performance is related to the MOF-derived porous structure. Furthermore, the $\text{F-Bi}_2\text{O}_3\text{-O}_v$ catalyst delivers higher formate selectivity and activity relative to $0.5\text{F-Bi}_2\text{O}_3\text{-O}_v$ and $2\text{F-Bi}_2\text{O}_3\text{-O}_v$ with different levels of fluorine doping [Supplementary Figure 24]. Although the highly crystalline Bi-O component in $\text{Bi}_2\text{O}_3\text{-O}_v$ serves as a key active site for promoting CO_2 to formate conversion, it fails to sustain high selectivity and stability at elevated potentials. Fluorination effectively addresses this drawback by generating Bi-F sites, which serve to optimize the reaction pathway and enhance formate selectivity. The $\text{F-Bi}_2\text{O}_3\text{-O}_v$ catalyst exhibits high durability, maintaining a formate FE greater than 90% during continuous electrolysis for 25 h at a current density of 300 mA cm^{-2} [Figure 3D]. Moreover, the $\text{F-Bi}_2\text{O}_3\text{-O}_v$ catalyst

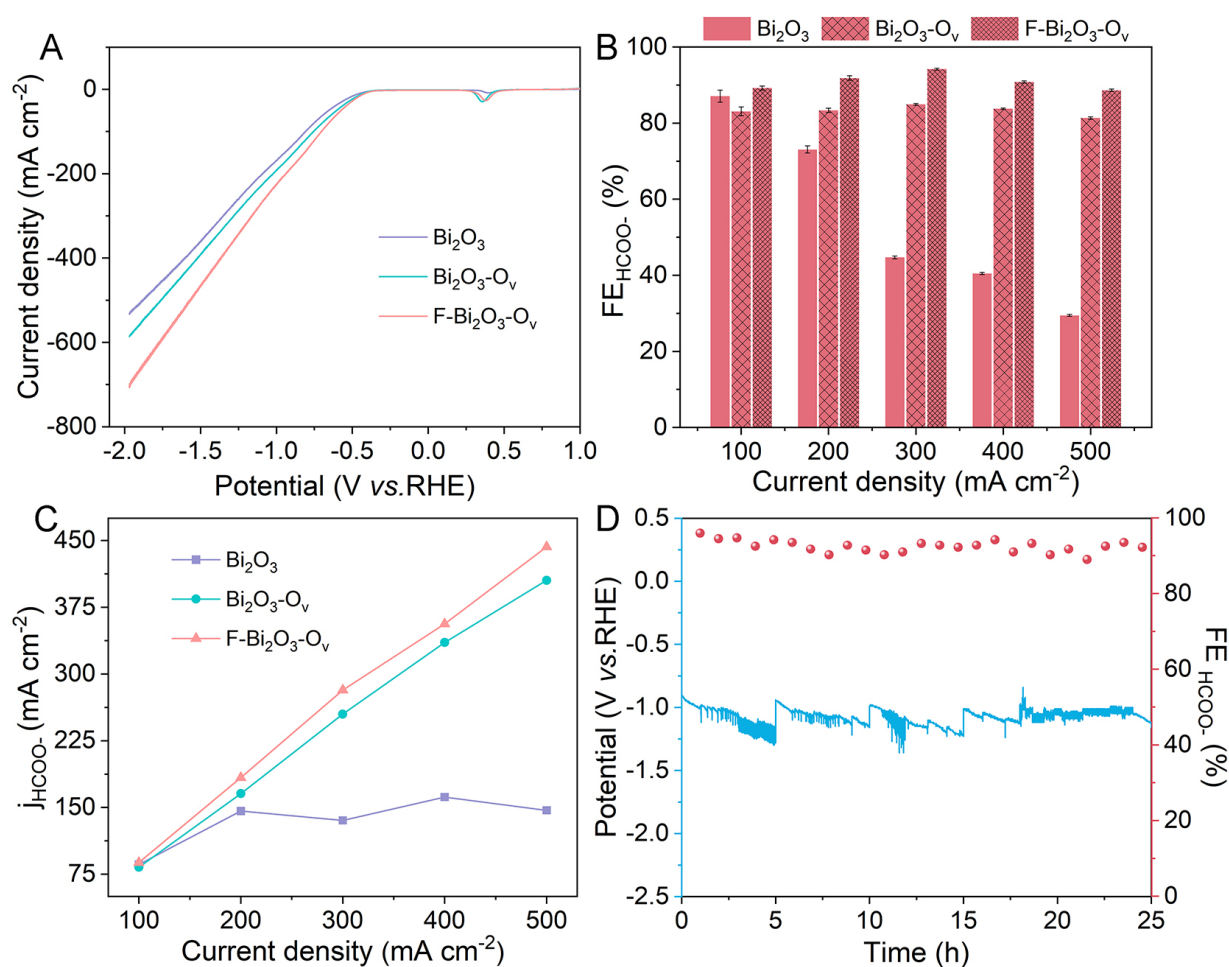


Figure 3. (A) LSV curves for Bi₂O₃, Bi₂O₃-O_v and F-Bi₂O₃-O_v in a CO₂-saturated 1 M KOH electrolyte at a scan rate of 5 mV s⁻¹. (B) Current-dependent formate FE for Bi₂O₃, Bi₂O₃-O_v and F-Bi₂O₃-O_v; the error bars represent the standard deviation of the mean of three independent replicates. (C) Partial current densities for Bi₂O₃, Bi₂O₃-O_v and F-Bi₂O₃-O_v under different current conditions. (D) Stability of F-Bi₂O₃-O_v at a current density of 300 mA cm⁻².

delivers a far superior partial current density and product selectivity at comparable potentials to previously reported Bi-based electrocatalysts [Supplementary Table 1]. The XRD analysis confirms that the Bi₂O₃ component in the used F-Bi₂O₃-O_v catalyst is maintained after the long-term CO₂ reduction tests [Supplementary Figure 25]. The XPS analysis of the used F-Bi₂O₃-O_v catalyst also confirms the presence of Bi³⁺ species [Supplementary Figure 26A]. These results account for the high electrocatalytic stability. In addition, the concentration of oxygen vacancies is unchanged following the reaction [Supplementary Figure 26B]. The fluorine doping stabilizes the oxygen vacancies in the Bi₂O₃ lattice under reductive potentials, preserving catalytic activity. Furthermore, the SEM and TEM images reveal that the catalyst retains its original morphology following electrolysis [Supplementary Figures 27 and 28].

The overpotentials at various current densities were systematically analyzed [Supplementary Figure 29] to evaluate the influence of the local environment in modulating the reaction energy barrier. At a current density of 100 mA cm⁻², the F-Bi₂O₃-O_v catalyst requires a potential of -0.48 V (vs. RHE) to drive the CO₂ reduction reaction toward formate production. In the high current density region (> 200 mA cm⁻²), F-Bi₂O₃-O_v demonstrates lower overpotentials when compared with Bi₂O₃-O_v and Bi₂O₃ [Supplementary Figures 30–32]. This suggests that the fluorine doping effectively reduces the activation

energy barrier for CO₂ electroreduction. Electrochemical impedance spectroscopy (EIS) analysis [Supplementary Figure 33] shows that F-Bi₂O₃-O_v exhibits a smaller charge transfer resistance than Bi₂O₃-O_v and Bi₂O₃. This indicates an enhanced rate of interfacial charge transport, facilitating the rapid generation of reaction intermediates. The electrochemically active surface area (ECSA) was assessed in double-layer capacitance (Cdl) measurements [Supplementary Figure 34]^[39]. Both F-Bi₂O₃-O_v and Bi₂O₃-O_v exhibit higher Cdl values than Bi₂O₃, which can be attributed to a greater dispersion and increased exposure of active sites in the Bi₂O₃-O_v materials [Supplementary Figure 35]. A Tafel analysis was performed [Supplementary Figure 36] to gain a better understanding of the reaction kinetics. The Tafel slope for Bi₂O₃-O_v (164.9 mV dec⁻¹) is lower than that of Bi₂O₃ (242 mV dec⁻¹), indicating that the oxygen vacancies primarily enhance CO₂ activation. Moreover, F-Bi₂O₃-O_v (151.5 mV dec⁻¹) exhibits the lowest Tafel slope, demonstrating that fluorine doping serves to promote interfacial charge transfer. This synergistic integration effectively reduces the energy barrier for key intermediate formation.

In situ ATR-FTIR analysis was employed to investigate the reaction intermediates associated with CO₂ reduction over F-Bi₂O₃-O_v [Figure 4A]. The spectra collected at applied currents ranging from -100 to -500 mA, exhibit several distinct absorption features. The bands located at 1,623, 1,120 and 1,494 cm⁻¹ are assigned to vibrational modes of H₂O, adsorbed CO₃²⁻ and dissolved CO₃²⁻, respectively^[40,41]. The negative band at 1,237 cm⁻¹ corresponds to *CO₂ adsorbed at the electrolyte-catalyst interface^[42,43]. The evolution of this band with increasing current indicates an accelerated dissolution of adsorbed CO₂ and subsequent conversion to *OCHO. This mechanism is consistent with the emergence of a characteristic fingerprint peak for *OCHO near 1,397 cm⁻¹ and a progressive increase in intensity with increasing applied current^[44,45]. These findings demonstrate that the formation of *OCHO as the key intermediate on F-Bi₂O₃-O_v is highly responsive to variations in current. Density functional theory (DFT) calculations were performed to determine the source of enhanced catalytic activity. The (221) facet of Bi₂O₃ was selected as the theoretical model surface for both Bi₂O₃-O_v and F-Bi₂O₃-O_v based on the XRD and HRTEM results, where the (221) reflection is identified as the primary facet. The fluorine atom substitutes the lattice oxygen, resulting in the formation of Bi-F bonds and the generation of additional oxygen vacancies [Supplementary Figure 37]. The density of states (DOS) for F-Bi₂O₃-O_v exhibits the markedly higher electronic density near the Fermi level compared to Bi₂O₃-O_v, suggesting a superior electrical conductivity [Supplementary Figure 38]. As shown in the projected density of states (PDOS) in Figure 4B, a significant overlap of F 2p, O 2p and Bi 6p orbitals below the Fermi level indicates a strong interaction between F and Bi atoms. As a consequence of the high electronegativity of fluorine, the p-band center of Bi is shifted positively (from -0.450 to -0.367 eV), consistent with an increasing local electron density around Bi. The p-band center of O 2p is shifted to a higher energy (from -3.137 to -3.076 eV). This enhances the reactivity of oxygen sites and lowers energy of oxygen vacancies formation. The modified electronic redistribution optimizes the adsorption strength of reaction intermediates on Bi sites, leading to an enhanced catalytic activity.

The Gibbs free energy profiles for CO₂ reduction to formate and the corresponding intermediate adsorption configurations were constructed to evaluate the reaction thermodynamics [Figure 4C, Supplementary Figures 39 and 40]. The reaction pathway analysis identifies the conversion of the *OCHO intermediate to formate as the rate-determining step (RDS)^[33]. The calculations indicate that fluorine doping serves to optimize the adsorption strength of the key intermediate. The Gibbs free energy of *OCHO on F-Bi₂O₃-O_v is 1.43 eV, compared with 1.56 eV on Bi₂O₃-O_v. An optimized binding energy prevents an overly strong interaction of the intermediates on the pristine surface, lowering the RDS energy barrier. The theoretical findings confirm that fluorine doping acts as an electronic promoter and works synergistically with oxygen vacancies to provide a thermodynamically favorable pathway for efficient formate production.

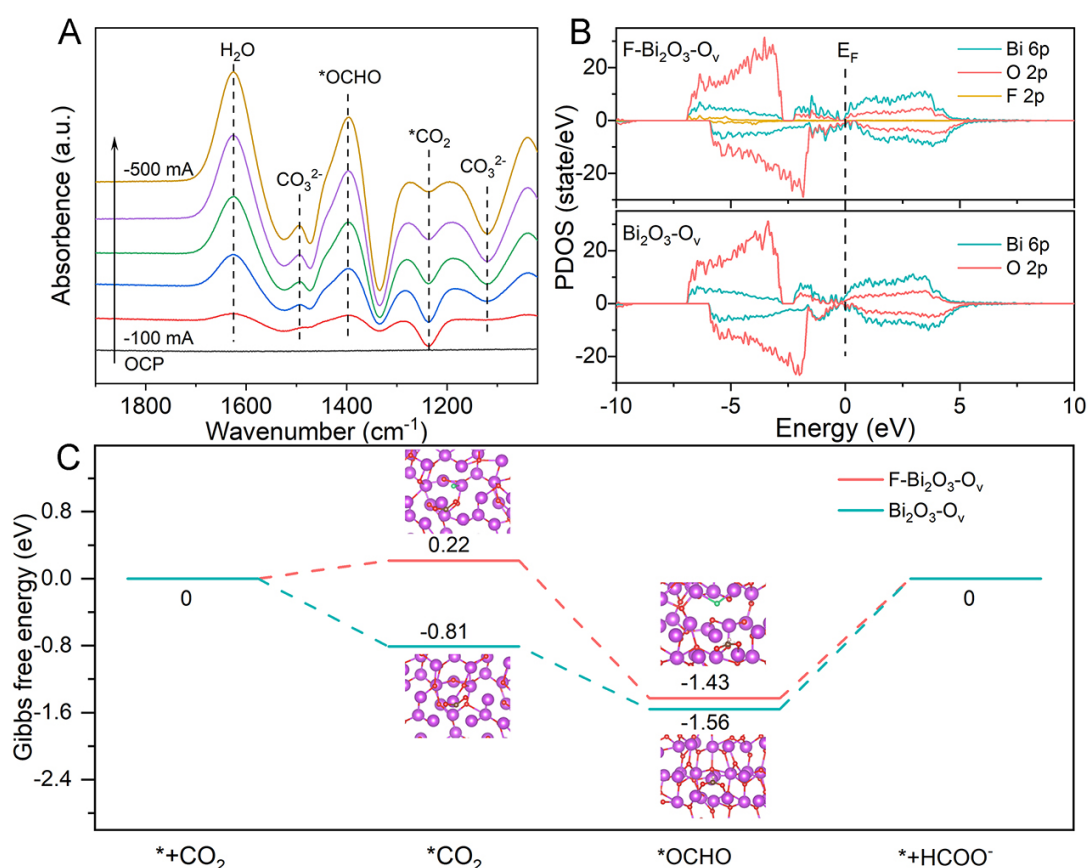


Figure 4. (A) *In situ* ATR-FTIR spectra of F-Bi₂O₃-O_v at different current densities. (B) PDOS for the Bi and O atomic p-orbitals in Bi₂O₃-O_v and Bi, O and F atomic p-orbitals in F-Bi₂O₃-O_v. (C) Gibbs free energy diagrams of the CO₂ to formate pathways on Bi₂O₃-O_v and F-Bi₂O₃-O_v with the adsorption configurations of the corresponding intermediates.

CONCLUSIONS

In conclusion, we have designed and synthesized fluorine-doped Bi₂O₃ catalysts with abundant oxygen vacancies via a fluoride-assisted pyrolysis of Bi-MOF. The catalysts deliver an efficient selective conversion of CO₂ to formate at industrial current densities. The combination of DFT calculations and experimental measurements has established the role of oxygen vacancies in promoting CO₂ activation. Fluorine doping optimizes the local electronic structure of Bi₂O₃, leading to a high-performance electrocatalytic generation of formate. The findings of this work can inform the design of doped metal-based catalysts. Moreover, the study offers new insights to the electrocatalytic reduction of CO₂ into value-added products.

DECLARATIONS

Authors' contributions

Conceptualization, methodology, investigation, formal analysis and writing (first draft): Qiao, Y.

Conceptualization, validation, writing-review and editing: Xu, Y.

Data provision, review and editing: Yang, J.

Data verification and manuscript revision: Ding, J.; Gu, X.

Availability of data and materials

The original contributions presented in this study are included in the article/[Supplementary Materials](#). Further inquiries can be directed to the corresponding author(s).

AI and AI-assisted tools statement

Not applicable.

Financial support and sponsorship

This work was supported by the National Natural Science Foundation of China (22162019, 22261040, 22462019), the Science and Technology Projects of Inner Mongolia Autonomous Region (2021GG0195) and the Natural Science Foundation of Inner Mongolia Autonomous Region (2021MS02017).

Conflicts of interest

All authors declared that there are no conflicts of interest.

Ethical approval and consent to participate

Not applicable.

Consent for publication

Not applicable.

Copyright

© The Author(s) 2026.

Supplementary Materials

[Supplementary Materials](#)

REFERENCES

1. Gidden, M. J.; Joshi, S.; Armitage, J. J.; et al. A prudent planetary limit for geologic carbon storage. *Nature* **2025**, *645*, 124-32. DOI PubMed PMC
2. O'Brien, C. P.; Miao, R. K.; Shayesteh Zeraati, A.; Lee, G.; Sargent, E. H.; Sinton, D. CO₂ electrolyzers. *Chem. Rev.* **2024**, *124*, 3648-93. DOI PubMed
3. Tyne, R. L.; Barry, P. H.; Lawson, M.; et al. Rapid microbial methanogenesis during CO₂ storage in hydrocarbon reservoirs. *Nature* **2021**, *600*, 670-4. DOI PubMed PMC
4. Wang, H.; Kang, X.; Han, B. Optimizing CO₂ electroreduction: theoretical insights for enhancing efficiency across elementary steps. *Chem. Soc. Rev.* **2025**, *54*, 10156-244. DOI
5. Ye, N.; Wang, K.; Tan, Y.; et al. Industrial-level CO₂ to formate conversion on Turing-structured electrocatalysts. *Nat. Synth.* **2025**, *4*, 799-807. DOI
6. Khan, B.; Faheem, M. B.; Peramaiah, K.; et al. Photoelectrochemical CO₂-to-formic acid conversions: advances in photoelectrode designs and scale-up strategies. *Adv. Energy. Mater.* **2025**, *16*, e04018. DOI
7. Huang, Q.; Qian, Z.; Ye, N.; et al. In situ reconstructed hydroxyl-rich atomic-thin Bi₂O₂CO₃ enables ampere-scale synthesis of formate from CO₂ with activated water dissociation. *Adv. Mater.* **2025**, *37*, 2415639. DOI
8. Chu, Y.; Yang, Y.; Cao, D.; et al. Regulating the rate-determining step of bismuth electrocatalysts by directional facet reconstruction for efficient CO₂ reduction. *Adv. Funct. Mater.* **2025**, *35*, 2508387. DOI
9. Chen, Z.; Xiao, Y.; Qiao, X.; et al. Monitoring chalcogenide ions-guided in situ transform active sites of tailored bismuth electrocatalysts for CO₂ reduction to formate. *Proc. Natl. Acad. Sci. USA.* **2025**, *122*, e2420922122. DOI PubMed PMC
10. Guo, W.; Cao, X.; Tan, D.; Wulan, B.; Ma, J.; Zhang, J. Thermal-driven dispersion of bismuth nanoparticles among carbon matrix for efficient carbon dioxide reduction. *Angew. Chem. Int. Ed.* **2024**, *63*, e202401333. DOI
11. Xiao, Y.; Liu, D.; Yang, J.; et al. Controllable reconstruction of β -Bi₂O₃/Bi₂O₂CO₃ composite for highly efficient and durable electrochemical CO₂ conversion. *Nano. Lett.* **2025**, *25*, 6548-55. DOI
12. Ren, X.; Liu, F.; Wu, H.; et al. Reconstructed bismuth oxide through in situ carbonation by carbonate-containing electrolyte for highly active electrocatalytic CO₂ reduction to formate. *Angew. Chem. Int. Ed.* **2024**, *63*, e202316640. DOI
13. Deng, P.; Wang, H.; Qi, R.; et al. Bismuth oxides with enhanced bismuth-oxygen structure for efficient electrochemical reduction of carbon dioxide to formate. *ACS. Catal.* **2020**, *10*, 743-50. DOI
14. Zhang, Y.; Zhang, G.; Song, Q.; et al. Spin-polarization in rigid/soft layered oxide catalyst regulates key intermediates for efficient CO₂-to-formate conversion. *Angew. Chem. Int. Ed.* **2026**, *65*, e17481. DOI

-
15. Chen, X.; Lu, R.; Li, C.; et al. Activating inert non-defect sites in Bi catalysts using tensile strain engineering for highly active CO₂ electroreduction. *Nat. Commun.* **2025**, *16*, 1927. DOI PubMed PMC
 16. Wang, S.; Yuan, X.; Zhou, S.; et al. Single-atomic-Ni electrocatalyst derived from phthalocyanine-modified MOF for conveying CO₂ intelligent utilization. *Energy Mater.* **2024**, *4*, 400032. DOI
 17. Wang, Y.; Li, G.; Feng, J.; et al. Boosting electrochemical CO₂ reduction to formate over La-doped SnO₂ via pinning effect and water activation. *J. Am. Chem. Soc.* **2025**, *147*, 40126-35. DOI
 18. Feng, J.; Wu, L.; Liu, S.; et al. Improving CO₂-to-C₂₊ product electroreduction efficiency via atomic lanthanide dopant-induced tensile-strained CuO_x catalysts. *J. Am. Chem. Soc.* **2023**, *145*, 9857-66. DOI
 19. Yang, X.; Wu, Z.; Li, Y.; et al. Atomically dispersed cerium on copper tailors interfacial water structure for efficient CO-to-acetate electroreduction. *Nat. Commun.* **2025**, *16*, 2811. DOI PubMed PMC
 20. Lei, H.; Yang, W.; Hu, S.; et al. Synergistic effect of boron and oxygen coordination on ruthenium clusters for industrial water splitting in alkaline medium. *Angew. Chem. Int. Ed.* **2025**, *64*, e202503871. DOI
 21. Wang, Q.; Dai, M.; Li, H.; et al. Asymmetric coordination induces electron localization at Ca sites for robust CO₂ electroreduction to CO. *Adv. Mater.* **2023**, *35*, 2300695. DOI
 22. Li, Y.; Zou, J.; Sun, L.; et al. Strong electronic interactions of the abundant Cu/Ce interfaces stabilized Cu₂O for efficient CO₂ electroreduction to C₂₊ products under large current density. *Adv. Funct. Mater.* **2025**, *35*, 2509899. DOI
 23. Huang, F.; Chen, X.; Sun, H.; et al. Atmosphere induces tunable oxygen vacancies to stabilize single-atom copper in ceria for robust electrocatalytic CO₂ reduction to CH₄. *Angew. Chem. Int. Ed.* **2024**, *64*, e202415642. DOI
 24. Chawla, G.; Dutta, N.; Kediya, S.; et al. Enhancing C₂₊ product faradaic efficiency in CO₂ reduction using fluorine-stabilized superhydrophobic copper (δ⁺). *J. Am. Chem. Soc.* **2025**, *147*, 38169-79. DOI
 25. Jia, C.; Tan, X.; Sun, Q.; et al. Fluorine doping-assisted reconstruction of isolated Cu sites for CO₂ electroreduction toward multicarbon products. *Adv. Mater.* **2025**, *37*, 2417443. DOI PubMed PMC
 26. An, X.; Li, S.; Yang, Z.; et al. F-doped In(OH)₃ for electrochemical reduction of CO₂ to formate. *Chem. Eng. J.* **2023**, *455*, 140720. DOI
 27. Yang, Y.; Gao, X.; Yang, S.; Shen, Y.; Xie, A. Synthesis and superior SERS performance of porous octahedron Cu₂O with oxygen vacancy derived from MOFs. *J. Mater. Sci.* **2021**, *56*, 9702-11. DOI
 28. Zhang, C.; Lin, Z.; Jiao, L.; Jiang, H. L. Metal-organic frameworks for electrocatalytic CO₂ reduction: from catalytic site design to microenvironment modulation. *Angew. Chem. Int. Ed.* **2024**, *63*, e202414506. DOI
 29. Ma, Y.; Zhang, G.; Yu, Q.; Lyu, S.; Duan, X.; Zhang, S. Heterogeneous nanoporous organic frameworks-based catalysts for electrochemical CO₂ reduction reaction. *Energy Mater.* **2025**, *5*, 500053. DOI
 30. Qi, Q.; Zhang, C.; Guo, T.; et al. Spatiotemporal control of MOF reconstruction unlocks efficient oxygen evolution. *Adv. Mater.* **2026**, *38*, e15800. DOI
 31. Su, Y.; Otake, K.; Zheng, J. J.; et al. Diffusion-rate sieving of propylene and propane mixtures in a cooperatively dynamic porous crystal. *Nat. Commun.* **2024**, *15*, 2898. DOI PubMed PMC
 32. Su, Y.; Otake, K.; Zheng, J. J.; Horike, S.; Kitagawa, S.; Gu, C. Separating water isotopologues using diffusion-regulatory porous materials. *Nature* **2022**, *611*, 289-94. DOI PubMed
 33. Liu, C.; Mei, B.; Shi, Z.; et al. Operando formation of highly efficient electrocatalysts induced by heteroatom leaching. *Nat. Commun.* **2024**, *15*, 242. DOI PubMed PMC
 34. Wang, J.; Tang, W.; Zhu, Z.; et al. Stabilizing lattice oxygen of Bi₂O₃ by interstitial insertion of indium for efficient formic acid electrosynthesis. *Angew. Chem. Int. Ed.* **2025**, *64*, e202423658. DOI
 35. Liu, W.; Zhai, P.; Li, A.; et al. Electrochemical CO₂ reduction to ethylene by ultrathin CuO nanoplate arrays. *Nat. Commun.* **2022**, *13*, 1877. DOI PubMed PMC
 36. Xin, Y.; Zhu, Q.; Gao, T.; et al. Photocatalytic NO removal over defective Bi/BiOBr nanoflowers: the inhibition of toxic NO₂ intermediate via high humidity. *Appl. Catal. B. Environ.* **2023**, *324*, 122238. DOI
 37. Yang, C.; Wang, R.; Yu, C.; et al. Engineering stable Cu⁺-Cu⁰ sites and oxygen defects in boron-doped copper oxide for electrocatalytic reduction of CO₂ to C₂₊ products. *Chem. Eng. J.* **2024**, *484*, 149710. DOI
 38. Deng, P.; Yang, F.; Wang, Z.; et al. Metal-organic framework-derived carbon nanorods encapsulating bismuth oxides for rapid and selective CO₂ electroreduction to formate. *Angew. Chem. Int. Ed.* **2020**, *59*, 10807-13. DOI
 39. Wang, X.; Zhang, Y.; Wang, S.; et al. Steering geometric reconstruction of bismuth with accelerated dynamics for CO₂ electroreduction. *Angew. Chem. Int. Ed.* **2024**, *63*, e202407665. DOI

40. Jia, B.; Chen, Z.; Li, C.; et al. Indium cyanamide for industrial-grade CO₂ electroreduction to formic acid. *J. Am. Chem. Soc.* **2023**, *145*, 14101-11. [DOI PubMed PMC](#)
41. Zheng, Z.; Zheng, X.; Wang, L.; et al. Harnessing electrocatalytic coupling of carbon dioxide and methanol for high-efficiency formic acid production. *Angew. Chem. Int. Ed.* **2025**, *64*, e202512078. [DOI PubMed PMC](#)
42. Zhu, S.; Jiang, B.; Cai, W.; Shao, M. Direct observation on reaction intermediates and the role of bicarbonate anions in CO₂ electrochemical reduction reaction on Cu surfaces. *J. Am. Chem. Soc.* **2017**, *139*, 15664-7. [DOI PubMed](#)
43. Delmo, E. P.; Wang, Y.; Song, Y.; et al. *In situ* infrared spectroscopic evidence of enhanced electrochemical CO₂ reduction and C-C coupling on oxide-derived copper. *J. Am. Chem. Soc.* **2024**, *146*, 1935-45. [DOI](#)
44. Ling, Z.; Yin, Y.; Ni, W.; et al. Efficient CO₂-to-HCOOH conversion at industrial current density in strong acid via synergistic water activation. *Adv. Funct. Mater.* **2025**, *36*, e29166. [DOI](#)
45. Han, N.; Sun, M.; Zhou, Y.; et al. Alloyed palladium-silver nanowires enabling ultrastable carbon dioxide reduction to formate. *Adv. Mater.* **2021**, *33*, 2005821. [DOI](#)

Disclaimer/Publisher's Note: All statements, opinions, and data contained in this publication are solely those of the individual author(s) and contributor(s) and do not necessarily reflect those of OAE and/or the editor(s). OAE and/or the editor(s) disclaim any responsibility for harm to persons or property resulting from the use of any ideas, methods, instructions, or products mentioned in the content.



© The Author(s) 2026. Open Access This article is licensed under a Creative Commons Attribution 4.0 International License (<https://creativecommons.org/licenses/by/4.0/>), which permits unrestricted use, sharing, adaptation, distribution and reproduction in any medium or format, for any purpose, even commercially, as long as you give appropriate credit to the original author(s) and the source, provide a link to the Creative Commons license, and indicate if changes were made.